Fabrication of Ag/La(OH)$_3$ Nanorod Framework Composites Through Dealloying for CO Oxidation

XIANGYANG LI,[1,2] LANJIE NIU,[2] XIAOLONG ZHANG,[3] DONG DUAN,[1] KUN LI,[1,4] and ZHANBO SUN [1,5]

1.—School of Science, MOE Key Laboratory for Non-Equilibrium Synthesis and Modulation of Condensed Matter, Key Laboratory of Shaanxi for Advanced Functional Materials and Mesoscopic Physics, Xi'an Jiaotong University, Xi'an 710049, People's Republic of China. 2.—Xi'an Institute of Electromechanical Information Technology, Xi'an 710065, People's Republic of China. 3.—Department of Engineering Mechanics, Shijiazhuang Tiedao University, Shijiazhuang 050043, People's Republic of China. 4.—Fengfan Co., Ltd., Baoding 071021, People's Republic of China. 5.—e-mail: szb@mail.xjtu.edu.cn

Ag/La(OH)$_3$ nanorod framework composites were fabricated by dealloying melt-spun Al-La-Ag alloys for CO oxidation. After the removal of Al from the precursory alloys, La(OH)$_3$ nanorods bonded with each other to form a novel three-dimension (3D) architecture with nanopores. When the dealloyed samples were calcined at 300°C, Ag nanoparticles (NPs) were in situ supported on the surface of the nanorods and simultaneously contact interfaces were generated between the Ag NPs and the La(OH)$_3$ nanorods. The large specific surface areas, unique 3D framework structure and active OH radicals were believed to contribute to the improvement of the catalytic activity for CO oxidation. The catalytic performance of Ag/La(OH)$_3$ composite was highly dependent on the Ag content and calcination temperature. CO oxidation studies showed that the nanorod composite calcined at 300°C exhibited higher activity for CO oxidation in comparison with the uncalcined sample and pure La(OH)$_3$ nanorods. The Ag/La(OH)$_3$ nanorod framework should be a promising catalyst for CO catalytic oxidation owing to the combination of novel nanostructures and functionalized particles.

INTRODUCTION

CO catalytic oxidation is one of the most important reactions in the field of heterogeneous catalysis and fuel cells.[1,2] Traditionally, noble-metal nanoparticles (NPs) supported on oxide catalysts are widely used to eliminate CO from emissions.[2–5] As a relatively inexpensive noble metal, Ag has become an important candidate for the catalytic reactions in recent years. Furthermore, Ag-supported catalysts have gained considerable attention due to their catalytic properties for CO oxidation.[6–9] The catalytic activity of Ag-based catalysts is highly dependent on the active species, the metal–support interaction, and the character of the support during the synthesis pretreatment and processing.[6,9–11] A good support candidate can not only effectively anchor the metal particles but also boost the catalytic performance. Nevertheless, Ag NPs loaded on a widely used oxide surface generally causes more serious aggregation and a lower dispersion of active species under the same conditions.[10] Therefore, much effort should be made to explore novel supporting materials as a new direction in the future design of Ag-supported catalysts for CO oxidation.

The catalytic properties of a supported system strongly depend on the types of supporting materials involved. In addition to metal oxide catalyst supports, researchers have been devoted to searching for new supporting materials, such as carbon nanotubes,[12] foam ceramics,[13] and molecular sieves.[10] Yousefi et al. reported that well-dispersed spherical Ag NPs deposited on multi-walled carbon nanotubes can reach approximately 100% CO conversion at 220°C. Kolobova et al.[10] reported that the chemical composition and properties of a Zeolite Socony Mobil-5 (ZSM-5) support significantly affected the catalytic activity of Ag-supported

samples. Especially, the study of hydroxides as new supporting materials has been of growing interest owing to its great promise for applications in many catalytic reactions.[11,14–19] Xie et al.[14] reported that CeO$_2$ nanorods embedded in a Ni(OH)$_2$ matrix exhibited good selectivity and stability for detecting glucose non-enzymatically owing to the synergetic effects of the two components. Hu et al.[17] reported that ultrathin nanoplates of cobalt–manganese layered double hydroxide were a highly active and stable oxygen evolution catalyst. Haruta[16] found that Au catalysts based on alkaline–earth metal hydroxides, such as Be(OH)$_2$ and Mg(OH)$_2$, showed extremely high catalytic activity towards CO oxidation at $-77°C$ due to the basicity of the support material. Recently, Wang et al.[11] demonstrated that Au NPs supported on Mg(OH)$_2$ displayed a superior catalytic performance because the generated CO$_2$ weakly bonded to the Mg(OH)$_2$ surface for the continuous CO oxidation in the low-temperature range. Thus, it is reasonable to expect that hydroxides should be promising support materials that can improve the catalytic activity of supported catalysts by maximizing the support effects.

La(OH)$_3$ nanorods have attracted intensive attention due to their unique structures, high specific surface areas and potential applications.[20–23] La(OH)$_3$ nanorods with unique electronic structures can form oxygen vacancies and supply hydroxyl groups, which are conducive to the improvement of catalytic activity.[13,21,24] It has been reported that the presence of Ag NPs in Ag/CeO$_2$ catalyst can promote the formation of active surface-absorbed oxygen species as well as the activated oxygen filling the oxygen vacancies, which can act as active sites for continued CO catalytic oxidation.[25] When active Ag NPs are highly dispersed in a three-dimensional (3D) La(OH)$_3$ nanorod framework, the unique structure formed of Ag/La(OH)$_3$ nanorods can significantly enhance the catalytic activity due to the strong synergetic effect between the active components.[13,21] Many methods, including solvothermal and hydrothermal, were utilized to develop pure La(OH)$_3$ nanorod materials.[22,24,26,27] However, very few approaches have enabled the design of La(OH)$_3$-based nanorod composites without the use of surfactants. Recently, dealloying has been employed to fabricate nanoporous metals and metal/oxide composites with various morphologies.[28–32] The nanoporous composites can be obtained via subsequent deposition, annealing treatment, internal oxidation, and the use of diverse alloys as precursors.[29,30,33] Various types of composite structures can be fabricated for catalytic reactions if alloy compositions or precursory materials are well designed. In our previous study, porous NiO/CeO$_2$ nanorod composites were fabricated by dealloying–annealing and they exhibited enhanced catalytic activity.[34] More recently, one-dimensional Cu-doped CeO$_2$ nanowires with high catalytic activity have been synthesized through a dealloying–annealing strategy.[35] Therefore, the construction of a new 3D Ag/La(OH)$_3$ nanorod catalyst with a framework structure via a dealloying strategy has been examined by first investigating the nanorod composite as a catalyst for CO oxidation.

Here, the use of a melt-spun Al-La-Ag alloy as a precursor in the one-step synthesis of 3D Ag/La(OH)$_3$ nanorod composites has been demonstrated for CO oxidation. A facile, green and economic dealloying method was employed for the large-scale preparation of La(OH)$_3$ nanorod frameworks with a porous structure at 80°C without any template or surfactant. Ag NPs were simultaneously in situ supported on the surface of the nanorods. After post-thermal annealing, phase transitions occurred in the composites, and the possible formation mechanism has been further discussed. The CO oxidation reaction served as a probe reaction to gain insight into the support effect. Ag/La(OH)$_3$ nanorods calcined at 300°C exhibited the best catalytic activity compared with the other calcined samples and bare La(OH)$_3$ nanorods. The sample calcined at 300°C with dispersed Ag NPs can not only provide enough active species but also, with low crystallinity, is beneficial to active hydroxyl groups participating in the catalytic reaction process.

EXPERIMENT AND METHODS

Preparation

Al$_{90-x}$La$_{10}$Ag$_x$ (x = 0 at.%, 1 at.%, 3 at.% and 5 at.%) alloys were prepared from pure Al (99.90 wt.%), pure Ag (99.90 wt.%) and pure La (99.99 wt.%) by arc-melting using high-purity Ar as the protective atmosphere. An amount of 4 g of the starting materials were arc-melted using a tungsten electrode in a water-cooled copper crucible, and the obtained ingots were re-melted four times. The homogeneous pre-alloyed ingot was inserted into a quartz tube and re-melted by high-frequency induction heating to the required temperature. After the metal solution was blown onto the surface of a single roller melt spinning with a speed of 33 m s^{-1} under a controlled argon atmosphere, melt-spun ribbons were obtained with thicknesses of approximately 20–40 μm and widths of about 3 mm.

The as-quenched ribbons were immersed in a 20 wt.% NaOH aqueous solution at room temperature for 3 h and then treated at 80°C for another 10 h. The dealloyed samples were rinsed with reverse osmosis water and dehydrated alcohol. The dealloyed ribbons were calcined at 200–700°C for 2 h under a pure O$_2$ atmosphere.

Characterization

X-ray diffraction (XRD) patterns were recorded on a Bruker D8 Advance diffractometer using Cu-Kα radiation at 20 kV and 40 mA. The thermal decomposition behavior was analyzed by

thermogravimetric (TG) and differential scanning calorimetry (DSC) on a NETZSCH STA 449 C instrument. Samples (20 mg) were heated to 1000°C in an aluminium sample boat at a heating rate of 10°C/min with a stream of O_2/Ar gas. The microstructures were characterized using a transmission electron microscope (TEM; JEM-2100 microscope) and a field emission scanning electron microscope (SEM; JSM-7000F microscope) equipped with an INCA X-Sight Oxford energy dispersive x-ray spectrometer (EDS). X-ray photoelectron spectroscopy (XPS) was performed by an Axis Ultra Kratos (UK) multifunctional spectrometer using monochromatic Al-Kα radiation (1486.6 eV). All peaks were corrected with C 1s as the reference. Nitrogen sorption isotherms were measured at -196°C using a Micromeritics ASAP 2020 system. The pore size distributions were calculated from the desorption branch of the isotherm using the Barrett–Joyner–Halenda algorithm.

Catalytic Evaluation

The catalytic activity of the Ag/La(OH)$_3$ catalysts for CO oxidation was evaluated at atmospheric pressure in a stainless steel tubular reactor configured in a tubular furnace, as described in our previous work.[34] Approximately 100 mg of the catalyst was packed in the tube for each test. After the pretreatment, the calcined catalysts were cooled from the pretreatment temperatures to room temperature in N_2. The reaction gas mixture consisting of 1% CO, 10% O_2 and 89% N_2 (vol) was passed through the catalyst bed at a total flow rate of 100 mL min^{-1} (60,000 h^{-1}). The gas flow rates were adjusted and controlled using mass flow controllers (Brooks 5850E). The concentration of the generated CO_2 and unreacted CO gases was analyzed online by a GC-7900 gas chromatograph equipped with a flame ionization detector. The CO conversion (%) was determined by the difference in CO concentration between the inlet and outlet gases.

RESULTS AND DISCUSSION

Phase Composition, Morphology and Microstructure

Figure 1a shows XRD patterns of the melt-spun and dealloyed ribbons. As shown in Fig. 1a, the $Al_{90}La_{10}$ and $Al_{87}La_{10}Ag_3$ ribbons are composed of the α-Al and La_3Al_{11} phases. Ag atoms existed in the α-Al lattice and formed an α-Al (Ag) solid solution. After dealloying, the diffraction peaks of La(OH)$_3$ appeared for both samples. In addition, weak peaks of Ag can also be found in the as-dealloyed $Al_{87}La_{10}Ag_3$. Figure 1b shows the TG and DSC curves of the as-dealloyed $Al_{87}La_{10}Ag_3$ ribbons between 50°C and 1000°C. It can be observed that the weight loss and the small endothermic peak between 50°C and 150°C are due to the removal of adsorbed water. The DSC curve shows an

exothermic peak from 150°C to 230°C owing to the crystallization of the amorphous portion in the sample.[36] The sharp weight loss between 230°C and 460°C, corresponding to a very strong endothermic peak, is caused by the thermal dehydration of La(OH)$_3$. It is suggested that the La(OH)$_3$ composites have been converted into LaOOH.[37,38] The TG curve showed a slight downward slope up to 700°C, indicating the formation and crystallization of La_2O_3. The TG/DSC curves of the as-dealloyed $Al_{90}La_{10}$ ribbons are provided (see supplementary Fig. S1) and displayed similar results. It is further confirmed that the endothermic peak at 942.7°C correlates to the melting temperature of Ag NPs. Therefore, La(OH)$_3$ decomposed to La_2O_3 via a two-step dehydration decomposition at 405°C and 500°C, which is in good accordance with the literature.[37,38]

Figure 2 shows the XRD patterns of dealloyed $Al_{87}La_{10}Ag_3$ ribbons calcined at different temperatures. The as-dealloyed ribbons and the sample calcined at 200°C are composed of Ag and La(OH)$_3$ with well-developed crystallinity. After the dealloyed ribbons were calcined at 300°C, the diffraction peaks of La(OH)$_3$ weakened. When the sample was annealed at 400°C, amorphous LaOOH formed, although it still contained small crystalline domains, as indicated by the weak XRD peaks. After calcination at a temperature over 600°C, LaOOH converted to La_2O_3, which is in agreement with the TG/DSC results.

Table SI displays the EDS results of the dealloyed $Al_{90-x}La_{10}Ag_x$ ($x = 0, 1, 3, 5$) ribbons, indicating that the La/Ag atomic ratios of the dealloyed samples were close to that of the precursor alloy (see supplementary Table SI). After the dealloyed $Al_{87}La_{10}Ag_3$ sample was calcined at 300°C, the EDS spectrum and XPS survey spectra for the surfaces of the Ag/La(OH)$_3$ were provided (see supplementary Fig. S2). The EDS result shows that atomic proportions of Ag, La and Al have no obvious changes before and after calcination. And the relative surface atomic compositions of Ag/La(OH)$_3$ obtained by XPS obtained by XPS are around 27.8 at.% for Ag and 72.2 at.% for La, respectively. No signals for Al were detected perhaps because few Al were distributed on the surface of sample.

Figure 3 shows the SEM and TEM images of the dealloyed $Al_{87}La_{10}Ag_3$ and the dealloyed ribbons at 300°C. The plan-view SEM images of dealloyed $Al_{87}La_{10}Ag_3$, as shown in Fig. 3a, exhibit abundant distributed nanorods with average diameters of 14 nm. The cross-sectional image showed that interconnected nanorods constructed a 3D framework structure with many pores (see Fig. 3d). After the dealloyed ribbons were calcined at 300°C, the morphology did not exhibit an obvious evolution (Fig. 3b and e). The TEM image in Fig. 3c also shows the nanorod framework structure, and some particles, as indicated by circles, can be seen. Figure 3f shows the high-resolution transmission
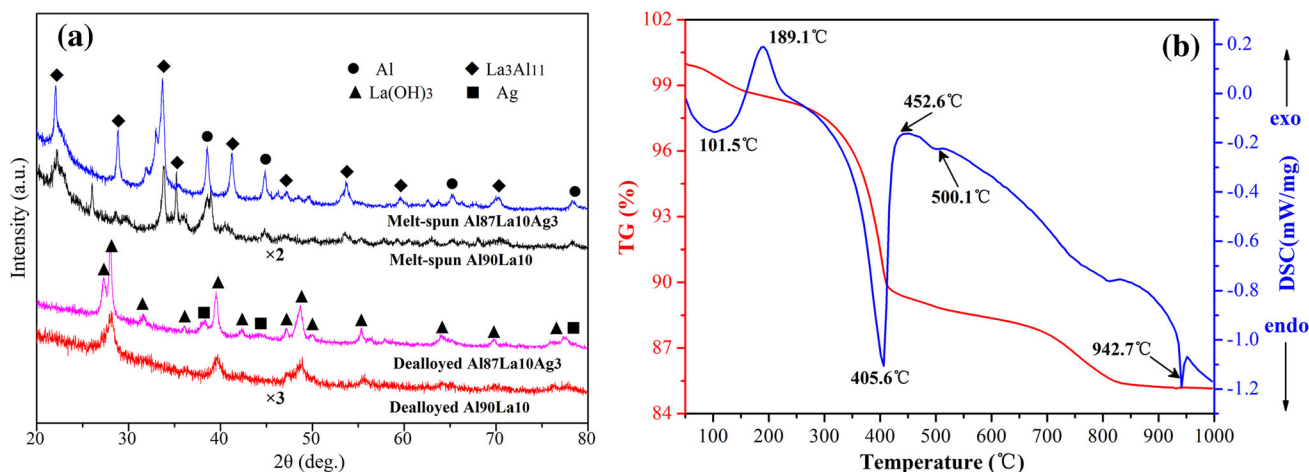
Fig. 1. XRD patterns of the Al$_{90}$La$_{10}$ and Al$_{87}$La$_{10}$Ag$_3$ ribbons before and after dealloying (a) and TG/DSC curves of as-dealloyed Al$_{87}$La$_{10}$Ag$_3$ ribbons (b).
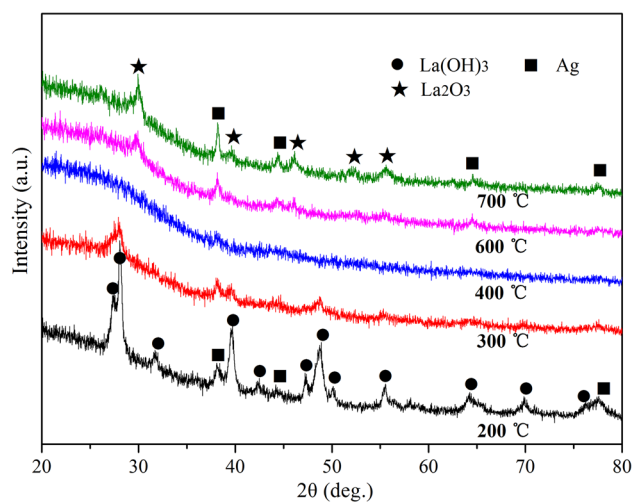

Fig. 2. XRD patterns of the as-dealloyed Al$_{87}$La$_{10}$Ag$_3$ ribbons calcined at 200–700°C.

electron microscope (HRTEM) image. The lattice fringes were measured to be 0.324 nm and 0.234 nm, corresponding to La(OH)$_3$(111) and Ag(111), respectively, indicating that the particles in Fig. 3c should be Ag NPs. It can also be observed that Ag NPs with diameters of approximately 10 nm are partly embedded on the surface of the La(OH)$_3$ nanorod, resulting in the formation of contact interfaces between them.

Chemical State of the Nanorod Composite

Figure 4 shows the XPS spectra in the La 3d and O 1 s regions. For the Ag/La(OH)$_3$ nanorods (Fig. 4-a), La 3d$_{5/2}$ and 3d$_{3/2}$ peaks at 835.2 eV and 851.9 eV were observed with a spin–orbit splitting of 16.7 eV, and were assigned to the La 3d component of La(OH)$_3$.[23] The high binding energies of the satellites at 838.6 eV and 855.4 eV can be attributed to the shake-up process due to the O 2p-La 4f charge

transfer.[24] After the dealloyed Al$_{87}$La$_{10}$Ag$_3$ was calcined at 400°C, the binding energy of the obtained Ag/LaOOH sample shifted to slightly the higher binding energy positions of 835.3 eV and 851.5 eV, respectively, which may be due to the transformation of La(OH)$_3$ to LaOOH with different state effects after further calcination.[39] As illustrated in Fig. 4b, the O 1 s XPS spectra for the Ag/La(OH)$_3$ samples can be fitted with two peaks at 531.6 eV and 532.9 eV, ascribed to La–O and the bonding oxygen species (e.g., OH$^-$), respectively.[24] For the Ag/LaOOH nanorods, there are three peaks, namely, 529.7 eV for lattice oxygen, 531.6 eV for surface oxygen and 532.9 eV for the bonding oxygen species.[39] These results demonstrate the presence of La(OH)$_3$ with the +3 oxidation state for the dealloyed sample calcined at 300°C and the co-existence of LaOOH and La$_2$O$_3$ for the sample calcined at 400°C.

Physical Properties

The N$_2$ sorption isotherms and pore size distribution of the La(OH)$_3$ nanorods and Ag/La(OH)$_3$ nanorod composite are shown in Fig. 5. The isotherms of both samples are type IV with H$_3$ hysteresis loops in a relative pressure range from 0.8 to 1.0 (Fig. 5a), which are typical characteristics of a mesoporous structure. This result indicates the interconnected mesoporosity and high pore connectivity in the framework. A wide distribution range of pore sizes from 2 nm to 100 nm can be observed in Fig. 5b. The Brunauer–Emmett–Teller (BET) specific surface area values and pore parameters are provided in Table I. The specific surface area of La(OH)$_3$ is higher than that of the Ag/La(OH)$_3$ nanorods due to the Ag NPs loaded on the nanorod surface and penetrating into pores, which was also seen for CeO$_2$-based nanorod composites.[34] The two samples showed similar pore volumes.
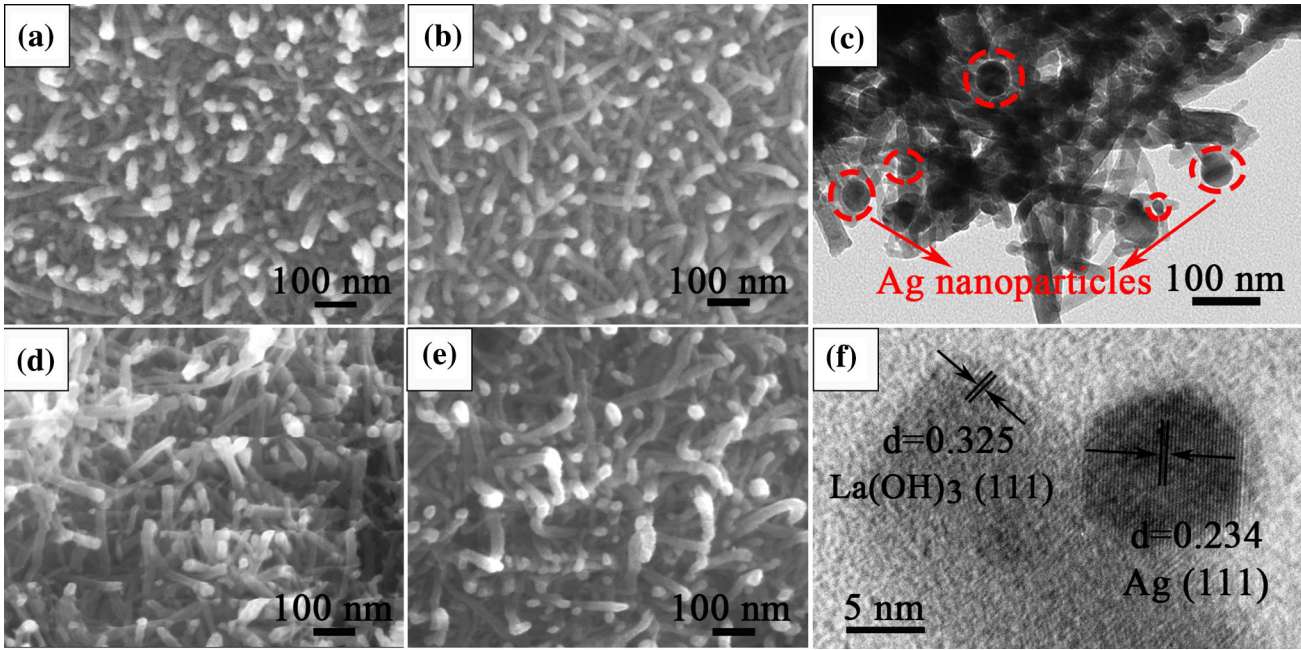
Fig. 3. Plan-view SEM images of the dealloyed $Al_{87}La_{10}Ag_3$ (a) and the dealloyed ribbons at 300°C (b). (d), (e) show the corresponding to section-view. TEM (c) and HRTEM (f) image of the dealloyed ribbons at 300°C.
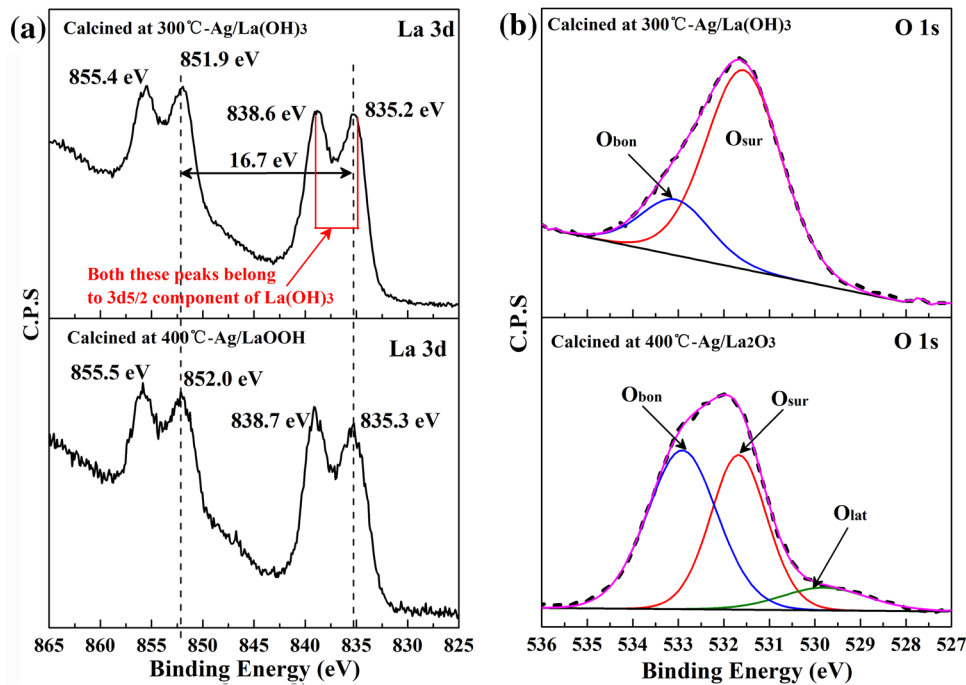

Fig. 4. La 3d (a) and O 1 s (b) XPS spectra of Ag/La(OH)$_3$ and Ag/LaOOH nanorod composites obtained from dealloyed $Al_{87}La_{10}Ag_3$ calcined at 300°C and 400°C, respectively.

Formation Mechanism of the Ag/La(OH)$_3$ Nanorod Composite

There is consensus that the active elements in precursors are easily selected for corrosion in a certain solution during the dealloying process.[40] After melt-spun Al-La-Ag ribbons were immersed in NaOH solution, the proposed reaction equations (Eqs. 1 and 2), as well as the corresponding Gibbs free energy at standard state are as follows. The reactions have negative values under giving conditions, indicating that the feasibility of the reaction.[41–43]

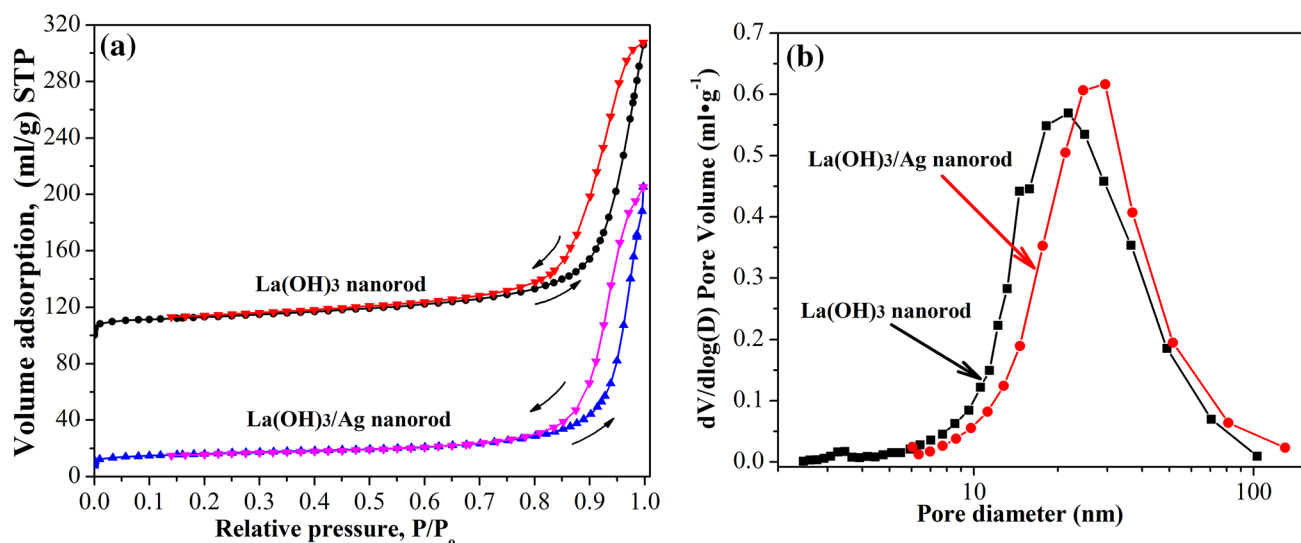$$2Al + 2NaOH + 2H_2O \rightarrow 2NaAlO_2 + 3H_2 \uparrow, \\ \Delta G° = -928.4 \text{ kJ/mol} \quad (1)$$
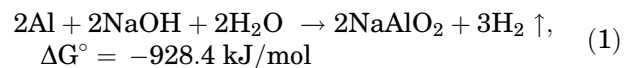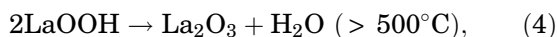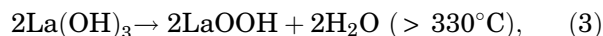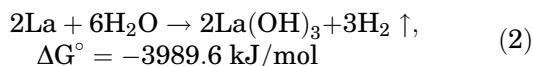
Fig. 5. N₂ adsorption–desorption isotherms (a) and the pore size curves (b) of the La(OH)₃ nanorod and Ag/La(OH)₃ nanorod composite.

Table I. The Brunauer–Emmett–Teller (BET) specific surface areas and pore parameters of the dealloyed Al₉₀La₁₀ and Al₈₇La₁₀Ag₃ calcined at 300°C

Dealloyed ribbons	BET surface area (m²/g)	Pore volume (cm³/g)	Pore size (nm)
$Al_{90}La_{10}$	49	0.32	25.9
$Al_{87}La_{10}Ag_3$	33	0.30	36.6

$$2La + 6H_2O \rightarrow 2La(OH)_3 + 3H_2 \uparrow, \quad \Delta G° = -3989.6 \text{ kJ/mol} \tag{2}$$

$$2La(OH)_3 \rightarrow 2LaOOH + 2H_2O \ (> 330°C), \tag{3}$$

$$2LaOOH \rightarrow La_2O_3 + H_2O \ (> 500°C), \tag{4}$$

Al atoms in the Al-La-Ag precursor first were etched in NaOH solution (Eq. 1). At the same time, La can react quite quickly with hot water to form La(OH)₃ and H₂ with considerable heat evolution of heat during the reaction (Eq. 2).[20] It has been reported that highly dispersive La(OH)₃ nanorods can be obtained in an alkaline solution with an appropriate basicity without using a template and surfactant.[26] The generated nanorods connect with each other, resulting in the formation of a nanorod framework. Moreover, aggregated Ag atoms formed Ag NPs that were in situ supported on the nanorod surface, which is similar to the result of the Ag/CeO₂ nanorods.[44] During calcination at 400°C, La(OH)₃ decomposed to LaOOH (Eq. 3) while maintaining the structural features of the La(OH)₃ nanorod. After the calcination temperature reached above 500°C, LaOOH dehydrated to form La₂O₃ (Eq. 4), which are in agreement with previous reports.[22,38,45] Therefore, the Ag/La(OH)₃ nanorod framework can be prepared by a facile dealloying method and can be transformed into stable Ag/

La₂O₃ with a nanorod morphology by subsequent calcination treatments.

Catalytic Performance Test

The catalytic oxidation test was carried out to evaluate the catalytic activity of La(OH)₃ and Ag/La(OH)₃ with different Ag contents. Figure 6 shows CO conversion as a function of temperature for Ag/La(OH)₃ samples obtained from dealloyed $Al_{90-x}La_{10}Ag_x$ (x = 0, 1, 3, 5) calcined at 300°C. After the catalysts were calcined at 300°C, the Ag/La(OH)₃ nanorods obtained from the dealloyed $Al_{87}La_{10}Ag_3$ displayed the fastest CO conversion rate. For comparison, bare La(OH)₃ nanorods displayed only 9.5% conversion of CO when the temperature increased to as high as 220°C, while the 3Ag/La(OH)₃ demonstrated almost complete conversion of CO. The CO catalytic activity can often be evaluated using the light-off temperature (T_{50}) and the 90% CO conversion temperature (T_{90}). Figure 6b shows the effect of the Ag content in the precursor alloys on the T_{50} and T_{90} values. The Ag-added catalyst exhibited much lower T_{50} and T_{90} values than the pure La(OH)₃ nanorods, which are the worst catalyst. The best performance was observed for the 3Ag/La(OH)₃ catalyst, from which T_{50} and T_{90} as low as 117°C and 175°C, respectively, were obtained. The results indicate that the addition of Ag contributed to the
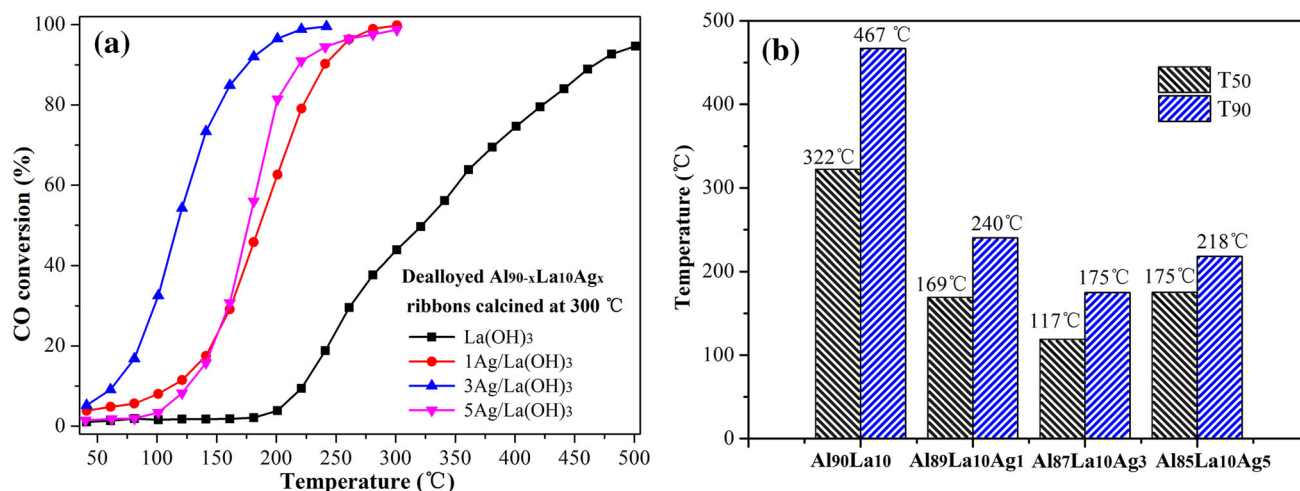
Fig. 6. CO conversion as a function of temperature for the La(OH)$_3$ and Ag/La(OH)$_3$ nanorod composite calcined at 300°C (a) and the variation in the temperature at 50% and 90% conversion between various Ag/La(OH)$_3$ catalysts (b).
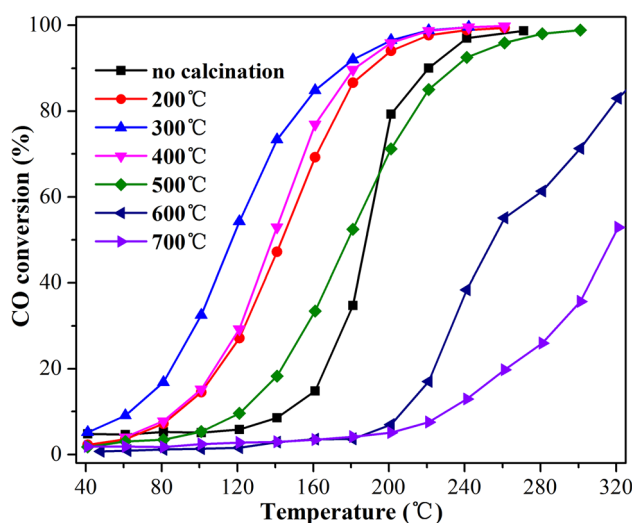

Fig. 7. CO conversion as a function of temperature for the dealloyed Al$_{87}$La$_{10}$Ag$_3$ nanorod composites calcined at 200–700°C.

improvement of catalytic activity and the Ag/La(OH)$_3$ nanorod catalyst obtained from Al$_{87}$La$_{10}$Ag$_3$ alloy can prominently enhance the catalytic activity for CO oxidation.

The calcination temperature dependence of the CO conversion rate is presented in Fig. 7. The light-off curves for the dealloyed Al$_{87}$La$_{10}$Ag$_3$ nanorod catalyst CO oxidation shifted to lower temperatures with the increase in calcination temperature. When the temperature reached 300°C, the obtained Ag/La(OH)$_3$ catalyst exhibited the best catalytic activity. After calcination at 400°C, the activity of Ag/LaOOH began to decline slightly. Furthermore, when the calcination temperature was further increased to 600°C and 700°C, the CO conversion of the generated Ag/La$_2$O$_3$ nanorod catalysts was only 87% and 52%, respectively, at a reaction

temperature of 320°C. Therefore, the calcination treatment has played an important role in the improvement of the catalytic activity due to the formation of three products at different temperatures (T), i.e., Ag/La(OH)$_3$ (< 400°C), Ag/LaOOH (400 < T < 500°C), Ag/La$_2$O$_3$ (> 500°C).

The catalytic activity of the as-prepared Ag/La(OH)$_3$ was sensitive not only to Ag content but also to the calcination temperature. The promoting effect of Ag was evident, together with the fact that the addition of Ag increases the CO conversion at a low Ag content, reaching a maximum and then declining. Moreover, the 3Ag/La(OH)$_3$ nanorods reached a maximum promoting effect, and their T_{50} temperature decreased to 117°C compared to that of the pure La(OH)$_3$ without Ag. When the 1 at.% Ag was added, the 10% CO conversion temperature around 120°C for 1Ag/La(OH)$_3$ was much higher that around 60°C for 3Ag/La(OH)$_3$ (see Fig. 6a), indicating that it cannot provide enough catalytic active species for the CO reaction. However, further increasing the Ag content was not beneficial for improving the catalytic activity. The TEM images of 5Ag/La(OH)$_3$ (see supplementary Fig. S3) show that there are still many dispersed Ag NPs supported on the nanorod surfaces. The loss in catalytic activity may be mainly due to high residual Al content (see supplementary Table SI), which is inactive and has a negative effect on the CO oxidation at low temperature. The atomic concentration of residual Al was approximately 22.8% for the dealloyed Al$_{85}$La$_{10}$Ag$_5$, which is considered to originate from the Al atoms buried within the Ag particles. In the investigated precursor composition, the negative resident Al content increased with the increased Ag content, especially for the 5Ag/La(OH)$_3$ catalysts, which may be responsible for its catalytic activity decline. Therefore, it is reasonable to assume that the 3Ag/La(OH)$_3$ catalyst with

dispersed Ag NPs can not only provide enough active species but also contain a low amount of negative residual Al, leading to higher activity than the others.

On the other hand, the calcination temperature has a significant influence on the dealloyed Ag/La(OH)₃ sample, and the thermal decomposition temperature affected the physical properties of the prepared support. The maximum catalytic activity providing 90% CO conversion at 175°C was obtained by the sample calcined at 300°C. The La(OH)₃ nanorod support with low crystallinity is beneficial to CO oxidation. However, calcination above 600°C caused a complete loss of catalytic activity due to the accompanying transformation of La(OH)₃ into La₂O₃ and the growth of Ag NPs, which was similarly reported in Au/La(OH)₃ and Au/MgOH catalysts.[46,47] SEM images of the dealloyed Ag/La(OH)₃ calcined at 700°C (see supplementary Fig. S4) illustrate large Ag particles on the surface of the La(OH)₃ nanorod framework due to the rapid growth at elevated temperature. Therefore, the highest catalytic performance for CO oxidation can be achieved from the dealloyed 3Ag/La(OH)₃ obtained from Al₈₇La₁₀Ag₃ calcined at 300°C.

It can be concluded that the Ag nanoparticles dispersed on the La(OH)₃ nanorod framework are the active species for CO oxidation. The hydroxide La(OH)₃ nanorod framework support plays a key role in the high catalytic activity. When the calcination temperature is above 300°C, the La(OH)₃ support is converted to LaOOH and La₂O₃, which was the mechanism of the nanorod shape-preserved transformation. However, the Ag/LaOOH and Ag/La₂O₃ catalysts showed lower catalytic activities, which may result from the support effect of the hydroxide. The temperature-dependent formation of hydroxyl groups participated in the catalytic reaction process. As explained in the literature,[11] the weak interaction of CO₂ with the Mg(OH)₂ surface can enhance continuous CO oxidation to avoid self-poisoning. Thus, active sites on the La(OH)₃ surface play a dominant role in the CO oxidation process. The Ag/La(OH)₃ samples prepared by the dealloying methods have a unique 3D nanorod framework structure with many exposed active sites. The interconnected large pores could enhance the transfer of the involved reaction species, and the nanopores could greatly increase the specific surface area to provide more active sites.

CONCLUSION

A Ag/La(OH)₃ nanorod framework with a porous structure can be fabricated through a facile dealloying strategy using an Al-La-Ag alloy as the precursor. The crystallinity and phase constitute of the dealloyed samples were regulated by heat treatments. After post-treatment at different temperatures, three nanorod composites were obtained: Ag/La(OH)₃ ($< 300°C$), Ag/LaOOH ($300 < T <$

$500°C$) and Ag/La₂O₃ ($T > 500°C$). When the dealloyed sample was calcined at 300°C, the Ag NPs were in situ deposited on the surface of La(OH)₃ with average diameters of 14 nm, creating strengthened interfaces between them. The T_{50} temperature of the Ag/La(OH)₃ nanorod composite was as low as 117°C. The nanorod catalyst exhibited enhanced catalytic performance for CO oxidation compared to bare La(OH)₃ and the corresponding dealloyed samples, owing to the high specific surface area and the unique nanorod framework structure with accessible pores and active sites on the inner surface. Our results can provide valuable information for the synthesis of noble-metal-supported La(OH)₃ and La₂O₃ composites.

ACKNOWLEDGEMENT

ELECTRONIC SUPPLEMENTARY MATERIAL

The online version of this article (https://doi.org/10.1007/s11837-018-3176-6) contains supplementary material, which is available to authorized users.

REFERENCES

1. L.Q. Qwabe, V.D.B.C. Dasireddy, S. Singh, and H.B. Friedrich, *Int. J. Hydrog. Energy* 41, 2144 (2016).
2. S. Royer and D. Duprez, *ChemCatChem* 3, 24 (2011).
3. J.R. Gaudet, A.D.L. Riva, E.J. Peterson, T. Bolin, and A.K. Datye, *ACS Catal.* 3, 846 (2013).
4. H. Shinjoh, *Catal. Surv. Asia* 13, 184 (2009).
5. H. Tanaka, M. Uenishi, M. Taniguchi, I. Tan, K. Narita, M. Kimura, K. Kaneko, Y. Nishihata, and J.I. Mizuki, *Catal. Today* 117, 321 (2006).
6. V.V. Dutov, G.V. Mamontov, V.I. Zaikovskii, and O.V. Vodyankina, *Catal. Today* 278, 150 (2016).
7. S. Bao, N. Yan, X. Shi, R. Li, and Q. Chen, *Appl. Catal. A Gen.* 487, 189 (2014).
8. X. Zhang, S. Cheng, W. Zhang, C. Zhang, N.E. Drewett, X. Wang, D. Wang, S.J. Yoo, J.G. Kim, and W. Zheng, *Ind. Eng. Chem. Res.* 56, 11042 (2017).
9. Z. Qu, F. Yu, X. Zhang, Y. Wang, and J. Gao, *Chem. Eng. J.* 229, 522 (2013).
10. E. Kolobova, A. Pestryakov, G. Mamontov, Y. Kotolevich, N. Bogdanchikova, M. Farias, A. Vosmerikov, L. Vosmerikova, and V.C. Corberan, *Fuel* 188, 121 (2017).
11. Y. Wang, D. Widmann, F. Lehnert, D. Gu, F. Schüth, and R.J. Behm, *Angew. Chem. Int. Ed.* 56, 9597 (2017).
12. N. Yousefi, M. Pazouki, M. Alizadeh, and F.A. Hesari, *Synth. React. Inorg. Met. Org. Chem.* 46, 464 (2016).
13. A. Pestryakov, E. Kolobova, and V. Lunin, *Int. J. Nanotechnol.* 13, 200 (2016).
14. Y. Li, P. Guan, F. Yu, W. Li, and X. Xie, *Nanomaterials* 7, 205 (2017).
15. G. Fan, F. Li, D.G. Evans, and X. Duan, *Chem. Soc. Rev.* 43, 7040 (2014).
16. M. Haruta, *J. New Mater. Electrochem. Syst.* 7, 163 (2004).

17. F. Song and X. Hu, *J. Am. Chem. Soc.* 136, 16481 (2014).
18. U.M. Patil, K.V. Gurav, V.J. Fulari, C.D. Lokhande, and O.S. Joo, *J. Power Sources* 188, 338 (2009).
19. F. Song and X. Hu, *Nat. Commun.* 5, 4477 (2014).
20. M. Méndez, J.J. Carvajal, L.F. Marsal, P. Salagre, M. Aguiló, F. Díaz, P. Formentín, J. Pallarès, and Y. Cesteros, *J. Nanopart. Res.* 15, 1 (2013).
21. X. Xiao, W. Zhang, J. Yu, Y. Sun, Y. Zhang, and F. Dong, *Catal. Sci. Technol.* 6, 5003 (2016).
22. P.S. Kohli, M. Kumar, K.K. Raina, and M.L. Singla, *J. Mater. Sci. Mater. Electron.* 23, 2257 (2012).
23. J.G. Kang, Y.I. Kim, D.W. Cho, and Y. Sohn, *Mater. Sci. Semicond. Process.* 40, 737 (2015).
24. F. Dong, X. Xiao, G. Jiang, Y. Zhang, W. Cui, and J. Ma, *Phys. Chem. Chem. Phys.* 17, 16058 (2015).
25. Y. Kang, M. Sun, and A. Li, *Catal. Lett.* 142, 1498 (2012).
26. J. Zhu, Z. Gui, and Y. Ding, *Mater. Lett.* 62, 2373 (2008).
27. B. Tang, J. Ge, C. Wu, L. Zhuo, J. Niu, Z. Chen, Z. Shi, and Y. Dong, *Nanotechnology* 15, 1273 (2004).
28. H. Yang, H. Qiu, J.Q. Wang, J. Huo, X. Wang, R.W. Li, and J. Wang, *J. Alloys Compd.* 703, 461 (2017).
29. T. Song, M. Yan, and M. Qian, *Corros. Sci.* 134, 78 (2018).
30. H.J. Qiu, J.Q. Wang, P. Liu, Y. Wang, and M.W. Chen, *Corros. Sci.* 96, 196 (2015).
31. N. Yu, T. Wang, C. Nie, L. Sun, J. Li, and H. Geng, *JOM* 68, 391 (2016).
32. N. Yu, L. Jiang, H. Hou, X. Chen, J. Li, H. Geng, and D. Zhao, *JOM* 69, 1027 (2017).
33. M.Y.N.K.C. Kima, W.T. Kimb, and D.H. Kima, *Corros. Sci.* 126, 381 (2017).
34. X. Zhang, K. Li, W. Shi, C. Wei, X. Song, S. Yang, and Z. Sun, *Nanotechnology* 28, 045602 (2016).
35. T. Kou, C. Si, J. Pinto, C. Ma, and Z. Zhang, *Nanoscale* 9, 8007 (2017).
36. R. Fiorenza, C. Crisafulli, G.G. Condorelli, F. Lupo, and S. Scirè, *Catal. Lett.* 145, 1691 (2015).
37. M. Ozawa, R. Onoe, and H. Kato, *J. Alloys Compd.* 408, 556 (2006).
38. A. Neumann and D. Walter, *Thermochim. Acta* 445, 200 (2006).
39. M.F. Sunding, K. Hadidi, S. Diplas, O.M. Løvvik, T.E. Norby, and A.E. Gunnæs, *J. Electron. Spectrosc.* 184, 399 (2011).
40. H.J. Qiu, L. Peng, X. Li, H.T. Xu, and Y. Wang, *Corros. Sci.* 92, 16 (2015).
41. M. Jung and B. Mishra, *J. Sustain. Metall.* 2, 1 (2016).
42. H. Senoh, M. Ueda, H. Inoue, N. Furukawa, and C. Iwakura, *J. Alloys Compd.* 266, 111 (1998).
43. J.A. Dean, *Lange's Handbook of Chemistry*, 15th ed. (New York: McGraw-Hill Book, 1999).
44. X. Zhang, G. Li, X. Song, S. Yang, and Z. Sun, *RSC Adv.* 7, 32442 (2017).
45. E. Füglein and D. Walter, *Zeitschrift fur anorganische und allgemeine Chemie* 632, 2154 (2006).
46. D.A.H. Cunningham, W. Vogel, H. Kageyama, S. Tsubota, and M. Haruta, *J. Catal.* 177, 1 (1998).
47. T. Takei, I. Okuda, K.K. Bando, T. Akita, and M. Haruta, *Chem. Phys. Lett.* 493, 207 (2010).